Materials Engineering in Perovskite for Optimized Oxygen Evolution Electrocatalysis in Alkaline Condition

Feifei Dong, Lu Li, Ziqi Kong, Xiaomin Xu, Yaping Zhang, Zhenghui Gao, Yangbiaokui Dong, Meng Ni, Quanbing Liu, and Zhan Lin**

Dr. F. Dong, L. Li, Z. Kong, Z. Gao, Y. Dong, Dr. Q. Liu, Prof. Z. Lin
Guangzhou Key Laboratory of Clean Transportation Energy Chemistry
School of Chemical Engineering and Light Industry
Guangdong University of Technology
Guangzhou Higher Education Mega Center
Guangzhou 510006, P. R. China
E-mail: liuqb@gdut.edu.cn; zhanlin@gdut.edu.cn

X. Xu
WA School of Mines: Minerals, Energy and Chemical Engineering (WASM-MECE)
Curtin University
Perth, WA 6102, Australia

Prof. Y. Zhang
State Key Laboratory of Environment-friendly Energy Materials
School of Materials Science and Engineering
Southwest University of Science and Technology
Mianyang 621010, P. R. China

Prof. M. Ni
Building Energy Research Group
Department of Building and Real Estate
The Hong Kong Polytechnic University
Hong Kong 999077, P. R. China

Keywords: electrocatalysis, oxygen evolution reaction, perovskites, water splitting, oxygen vacancy

Developing robust and highly efficient electrocatalysts for oxygen evolution reaction (OER) is critical for renewable, secure and emission-free energy technologies. Perovskite oxide $Ba_{0.5}Sr_{0.5}Co_{0.8}Fe_{0.2}O_{3-\delta}$ (BSCF) has emerged as a promising OER electrocatalyst with desirable intrinsic activity. Inspired by the factor that substituting heteroatom into transition-metal sublattice of perovskite can further optimize the OER activity, herein, we adopt nickel-substituted BSCF, i.e. $Ba_{0.5}Sr_{0.5}Co_{0.8-x}Fe_{0.2}Ni_xO_{3-\delta}$ (x = 0.05, 0.1, 0.2, denoted as BSCFNx, x = 5, 10, 20, respectively), as efficient and stable OER catalysts in alkaline solution. The phase structure, microchemistry, oxygen vacancy, and electrochemical activity of such samples are

well-investigated. The characterization results indicate that, endowed with a low overpotential of only 278 mV required for 10 mA cm^{-2} and a small Tafel slope of merely 47.98 mV dec^{-1}, BSCFN20 exhibits the optimum OER activity among this system, yielding a mass activity of 218.6 mA mg^{-1} and a specific activity of 1.68 mA cm^{-2} at 320 mV overpotential. When using BSCFN20 as an anode and Pt/C as a cathode to catalyze overall water splitting in 1 M KOH, the two-electrode configuration cell (BSCFN20||Pt/C) only requires a voltage of 1.63 V to achieve catalytic current density of 50 mA cm^{-2}, and the BSCFN20||Pt/C remains stable at 10 mA cm^{-2} for a duration of 80 h, which are superior to the state-of-the-art RuO_2||Pt/C counterpart. This work provides a feasible strategy for designing stable and highly active perovskite electrocatalysts for future electrochemical energy storage and conversion.

One of the main impediments for facilitating water splitting, metal-air batteries and regenerative fuel cell technologies lies in the kinetically sluggish oxygen evolution reaction (OER) process, which not only demands four sequential proton-coupled electron transfers, but also undergoes a transition of the spin states.[1-3] To improve the sluggish kinetics and motivate the reaction, a great many materials have been exploited as effective and efficient OER electrocatalysts. Metal oxides,[4,5] hydroxides,[6] metal chalcogenides,[7] organometallics,[8] and carbon-based materials[9,10] are recently identified as the most promising candidates. In particular, as one of the metal oxide electrocatalysts, functional perovskites (ABO_3) have received great attention due to their outstanding intrinsic activity, cost-effective character, large-scale implementation capability and environmentally friendly nature.[11,12] For instance, Shao-Horn's group proposed a volcano-shape diagram with e_g occupancy of surface transition metal in perovskite against OER activity.[13] The volcano curve manifests that $Ba_{0.5}Sr_{0.5}Co_{0.8}Fe_{0.2}O_{3-\delta}$ (BSCF) exhibits an optimal OER electroactivity in regards to precious metal-based IrO_2 benchmark approximately one order of magnitude higher, standing out from other perovskites as well as many advanced

materials. Since then, significant efforts have been dedicated to further optimizing the intrinsic activity of BSCF electrocatalyst for OER regarding its tremendous potential in energy storage and conversion applications.[14-16]

In general, combining several functional materials could provide a prospective approach to synergistically optimize the OER electroactivity. For example, it was reported that CoNi/BSCF/N-doped-C composite demands for only a low overpotential of 320 mV to reach a specific current density of 10 mA cm^{-2}, outperforming pristine BSCF (470 mV) and other predominant electrocatalysts.[17] Meanwhile, the OER performance was found to be closely associated with the morphology of the transition-metal oxides. Chen et al. successfully fabricated an amorphous BSCF nanofilm and achieved the two orders of magnitude enhancement in OER activity relative to its crystalline counterpart.[18] Thermal treatment in special atmosphere has also emerged as a desirable avenue to improve the electroactivity of BSCF. It was revealed that exposing BSCF to CO_2 atmosphere during heating could induce the *in-situ* formation of decorative carbonate layer on the surface, providing enhanced OER performance.[19] Recently, oxygen vacancies have been proven to profoundly enhance the electrocatalytic activity and durability of OER,[20-22] since oxygen vacancies can not only enhance the electrical conductivity of the catalyst, but also tailor the surface electronic structure and number of active sites for electrochemical reactions.[23] Furthermore, substituting heteroatoms into perovskites is quite facile to generate the favorable oxygen vacancies, thereby enhancing the electrochemical properties. Following this, F substituted BSCF (F-BSCF),[24] $La_x(Ba_{0.5}Sr_{0.5})_{1-x}Co_{0.8}Fe_{0.2}O_{3-\delta}$ (LBSCF),[25] and $Bi_{0.1}(Ba_{0.5}Sr_{0.5})_{0.9}Co_{0.8}Fe_{0.2}O_{3-\delta}$ (BBSCF)[26] were spotlighted as highly effective OER catalysts based on the doping engineering. Although these A-site and O-site doping strategies effectively enhance the OER performance of BSCF, B-site coordinated with O anions in perovskites generally stands as the active sites for oxygen-related reaction intermediates. Accordingly, substituting elements into B-site of BSCF

perovskite framework is supposed to more efficiently improve the OER electrocatalytic activity. Among the various B-site dopants, Ni cations are considered to be promising substitution candidates for benefiting the catalytic process of oxygen-related reaction.[27-29]

Herein, for the first time, we apply a series of B-site Ni-doped BSCF to oxygen evolution electrocatalysis in alkaline condition. BSCF specimens doped with different contents of Ni, namely $Ba_{0.5}Sr_{0.5}Co_{0.8-x}Fe_{0.2}Ni_xO_{3-\delta}$ (x = 0.05, 0.1, 0.2, denoted as BSCFNx, x = 5, 10, 20), were synthesized by a simple sol-gel method and characterized in terms of crystal structure, valence state of metal ions, oxygen non-stoichiometry, and electrochemical nature. The incorporation of Ni promotes the formation of oxygen vacancies, and the concentration of oxygen vacancies increases with the increment of Ni content without compromising the crystal structure. As we demonstrate, the optimum BSCFN20 catalyst only requires a low overpotential of 278 mV to deliver a current density of 10 mA cm^{-2} for OER, surpassing those of BSCF matrix and commercial RuO_2 benchmark. Together, this catalyst displays favorable OER performance with a mass activity of 218.6 mA mg^{-1} and a specific activity of 1.68 mA cm^{-2} at 320 mV overpotential. To push forward the practical application of the developed perovskite, a two-electrode electrolyzer with BSCFN20 as an anode and Pt/C as a cathode presents a cell voltage of only 1.63 V at 50 mA cm^{-2}, much lower than that of commercial RuO_2||Pt/C couple. In addition, the BSCFN20||Pt/C electrolyzer also exhibits remarkable long-term durability over 80 h of electrolytic water oxidation.

Substituting nickel into BSCF, despite the variation of the doping concentration, is capable of maintaining the typical perovskite structure as evidenced by XRD profiles in **Figure 1**a. Rietveld refinements (Figure S1, Supporting Information and Figure 1b) conducted on the XRD data to acquire structural information reveals that the three specimens crystallize in the cubic-symmetry structure with a space group of $Pm\overline{3}m$. The close agreement between the experimental data and calculating results demonstrates the proper selection of the structural

model. Detailed refinement information is summarized in Table S1 (Supporting Information). Figure 1c shows a typical HR-TEM image of BSCFN20, which clearly reveals well-visible lattice fringes with the interplanar *d*-spacing of 0.282 nm, agreeing well with the (110) crystalline plane. The inset in Figure 1c is the corresponding fast Fourier transformed (FFT) showing the angle of ~35° between the sets of lattice planes, indicative of a cubic lattice viewed along [$1\bar{1}0$] zoon axis, which is consistent with the XRD refinement analysis. Similar results are also observed for BSCFN5 and BSCFN10 (Figure S2, Supporting Information). EDX mappings (Figure 1d) confirm the concurrent existence of Ba, Sr, Co, Fe, and Ni and the homogeneous distribution of the elements in BSCFN20 sample. As noted above, the BSCFN*x* samples adopt a cubic crystal structure with the highest symmetry in the perovskite system, maximizing the transport and diffusion property of oxygen and electron, and thereby the OER activity.

XPS technique was taken to probe the chemical states of surface composition in studied samples. The XPS spectra of BSCFN*x* are presented in **Figure 2** and S3 (Supporting Information). Typically, simultaneous deconvolution for Co 2p and Ba 3d spectra is required in (Ba, Co)-containing perovskites due to the overlap of Co 2p and Ba 3d peaks.[30] Regarding Figure 2a, the peaks near 780 eV corresponds to Co $2p_{3/2}$ and Ba $3d_{5/2}$, while the binging energy at around 795 eV is ascribed to Co $2p_{1/2}$ and Ba $3d_{3/2}$. Although it is challenging to clearly distinguish the valence state of Co due to the overlapped spectra, the weak satellite peaks at around 788 eV manifest the dominance of Co^{3+} on the surfaces of all BSCFN*x* samples, which is of great significance to the OER in alkaline condition.[11,31] Besides, the shift toward the high binding energy is detected for Co $2p_{3/2}$ and $2p_{1/2}$ with increasing Ni content. Such shift can be attributed to the increase in Co^{2+} ion content.[32] As for Sr 3d spectra in Figure S3a (Supporting Information), the peaks at ~133.5 and ~135.3 eV are ascribed respectively to the Sr $3d_{5/2}$ and $3d_{3/2}$. The Fe 2p spectra display a doublet at ~711 and ~724 eV, as can be assigned to Fe $2p_{3/2}$

and $2p_{1/2}$ signals, respectively (Figure S3b, Supporting Information). In contrast to Co, no distinct variation in the surface Fe state is observed. As shown in Figure 2b, the spectra for dopant Ni consist of two main peaks and a satellite peak. The peaks located at binding energies of ~857 and ~874 eV arise from Ni $2p_{3/2}$ and $2p_{1/2}$ respectively, together with the satellite peak located at ~862 eV. The Ni-rich surface can benefit the facile formation of NiOOH as the redox-active sites, thereby facilitating the OER catalytic reaction.[33,34]

Notably, as shown in Figure 2c, the O 1s spectra are featured by four subordinate peaks located at 529.1 eV (lattice oxygen O^{2-}), 530.5 eV (highly oxidative oxygen O_2^{2-}/O^-), 531.5 eV (hydroxyl groups or surface-adsorbed oxygen OH^-/O_2), and 532.4 eV (adsorbed molecular water H_2O). Both highly oxidative oxygen O_2^{2-}/O^- and hydroxyl groups OH^- are closely associated with the oxygen defect.[35] The existence of oxygen defect could potentially facilitate oxygen incorporation and transport, thus enabling highly efficient OER electrocatalysis. Although the concentration of highly oxidative oxygen O_2^{2-}/O^- of BSCFN20 is inferior to those of BSCFN5 and BSCFN10, its hydroxyl groups OH^- significantly exceed the other two, signifying the possible existence of large amount of oxygen vacancies.

To quantificationally compare the concentration of oxygen deficiency for all studied samples, iodometric titration method was employed. According to the determination results, the oxygen non-stoichiometry (δ) increases with increasing Ni dopant content. The corresponding values for BSCFN5, BSCFN10, and BSCFN20 are 0.3, 0.35, and 0.44, respectively, much higher than those of BSCF matrix and other cobalt-based perovskites.[36-38] Such a significantly high δ value of BSCFN20 is expected to be beneficial for the occurrence of oxygen absorption and release, subsequently promoting the oxygen electrocatalytic activity.

The electrocatalytic performances of BSCFN*x* (*x* = 5, 10, 20) toward OER in 0.1 M KOH solution were evaluated by LSVs at 1600 rpm in a typical three-electrode system. All potentials given are referenced to RHE using the calibration equation emerged in the experimental section.

To distinguish the superiority of Ni-doped catalysts, the benchmark BSCF and RuO_2 were also performed with the similar measurements for comparison. The polarization curves in **Figure 3**a demonstrate that BSCFN20 electrode displays the optimal OER catalytic activity among all studied samples, delivering a low overpotential of 278 mV at 10 mA cm^{-2}. The overpotentials of BSCF and RuO_2 are 38 and 31 mV higher than that of BSCFN20, indicative of the significant effectiveness of Ni doping. In addition, the electrocatalytic activity improves as the doping ratio of Ni increases, manifested by the higher overpotentials of BSCFN5 (304 mV) and BSCFN10 (297 mV). With the hope of further enhancing electrocatalytic OER performance, attempts to introduce a greater level of Ni doping (x = 0.3) results in a failure to obtain a single-phase perovskite structure (Figure S4, Supporting Information), demonstrating the optimal doping ratio of x = 0.2. More convincingly, the comparison of overpotentials of BSCFN20 and other advanced perovskite electrocatalysts for OER at the current density of 10 mA cm^{-2} is summarized in **Table 1**. The satisfactory catalytic activity of BSCFN20 can be attributed to the much higher content of oxygen vacancies existing in the lattice. The intrinsic OER activity of BSCFN20 remains prominent even considering the experimental uncertainty, with a much higher current density than RuO_2 under the same voltage as shown in Figure 3b. Each data point displayed in the diagram is averaged from three independent measurements, and the errors bars indicate the standard deviation of the mean.

As an inherent parameter to assess the OER reaction kinetics of catalysts, the Tafel slope is derived from LSV polarization curves by plotting iR-corrected potential against logarithm of current density (Figure 3c). As expected, the Tafel slope for BSCFN20 is calculated to be 47.98 mV dec^{-1}, clearly smaller than those of other species (51-64 mV dec^{-1}), further evidencing the fast OER kinetics. Moreover, Figure 3d in the form of bar graph illustrates the mass activity (MA, mA mg^{-1}) and specific activity (SA, mA cm^{-2}) of BSCFNx catalysts, normalized by the oxide mass loading and BET surface area (Figure S5, Supporting Information) at η = 320 mV,

specifically. It is apparent that both MA and SA can considerably improve with an increase in doping concentration of Ni. Particularly, the BSCFN20 catalyst achieve a factor of more than 2 enhancement in both MA (218.6 mA mg^{-1}) and SA (1.68 mA cm^{-2}) for OER relative to pristine BSCF and other BSCFN*x* counterparts, implying its potential practical applications (credited to higher MA) and remarkably superior intrinsic activity (ascribed to higher SA).

Inspired by the bright prospect of BSCFN20 for OER performance, an electrocatalysis cell with commercial Pt/C as a cathode and BSCFN20 electrocatalyst as an anode (denoted as BSCFN20||Pt/C) was assembled for overall water splitting in 1 M KOH electrolyte. RuO_2||Pt/C cell was also prepared for comparison and the mass loading for all studied electrodes was 3 mg cm^{-2}. The corresponding linear volt-ampere curves shown in **Figure 4**a well prove the prominent practicability of BSCFN20 catalyst. At room temperature, BSCFN20||Pt/C affords a superior activity for overall water splitting with a cell voltage of only 1.63 V to support a current density of 50 mA cm^{-2}, evidently outperforming the references RuO_2||Pt/C couple (1.70 V) and $SrCo_{0.9}Ru_{0.1}O_{3-\delta}$||Pt/C couple (~1.72 V).[48] From a representative snapshot of the operating BSCFN20||Pt/C cell, given as the inset of Figure 4a, the clearly visible oxygen and hydrogen bubbles are continuously generated from the respective electrodes at 10 mA cm^{-2}. In addition to the catalytic activity, the stability of the cells is also critical for the commercial application. The long-term durability of the two-electrode cells was assessed by chronopotentiometry test. As seen in Figure 4b, notably, BSCFN20||Pt/C yields an almost steady potential during continuous oxygen and hydrogen production at a constant current density of 10 mA cm^{-2} for 80 h, whereas an obvious degradation of potential is observed for RuO_2||Pt/C after 80 h testing, demonstrating excellent electrocatalytic durability of two-electrode system BSCFN20||Pt/C for overall water splitting. The above outcome reveals that BSCFN20 holds significant promise in the field of energy conversion and storage, including electrochemical water splitting, fuel cells, and rechargeable metal-air batteries, etc.

In summary, we have demonstrated that substituting nickel into BSCF perovskite is a feasible and efficient approach to enhance the OER intrinsic activity. A series of doped BSCF perovskites $Ba_{0.5}Sr_{0.5}Co_{0.8-x}Fe_{0.2}Ni_xO_{3-\delta}$ (x = 0.05, 0.1, 0.2), labeled as BSCFNx (x = 5, 10, 20), are investigated in detail. The boosted OER electrocatalytic activity of BSCFNx is achieved with increasing doping level of Ni. As a result, the most active electrocatalyst BSCFN20 provides exceptional electrocatalytic performance with a low overpotential of 278 mV at 10 mA cm^{-2} and a small Tafel slope of 47.98 mV dec^{-1}, superior to those of the pristine BSCF and benchmark precious-metal-based RuO_2. Relative to the pristine BSCF, the BSCFN20 catalyst exhibits a factor of more than 4 and 7 increase in mass activity and specific activity for OER, respectively. The promising electroactivity can be ascribed to the increased oxygen vacancies resulted from the nickel substitution. Moreover, a two-electrode electrolyzer composed of BSCFN20 anode and Pt/C cathode in 1 M KOH electrolyte requires a voltage of only 1.63 V to drive a current density of 50 mA cm^{-2} and exhibits impressive durability at constant 10 mA cm^{-2} current density for a duration of 80 h, which are more competitive than that of the precious RuO_2||Pt/C catalytic couple for overall water splitting. The distinguished OER activity and durability demonstrate the tremendous potential of BSCFN20 perovskite in electrocatalysis and other sustainable energy technologies.

Supporting Information

Supporting Information is available from the Wiley Online Library or from the author.

Acknowledgements

This work was financially supported by a startup R&D funding from One-Hundred Young Talents Program of Guangdong University of Technology, China (No. 220413180), a Foundation for Youth Innovative Talents in Higher Education of Guangdong Province, China

(No. 2018KQNCX060), Joint Funds of Basic and Applied Basic Research Foundation of Guangdong Province, China (No. 2019A1515110322), a grant from National Natural Science Foundation of China (No. 21975056), grants from Research Grant Council, University Grants Committee, Hong Kong SAR (No. PolyU 152214/17E and PolyU 152064/18E).

Received: ((will be filled in by the editorial staff))
Revised: ((will be filled in by the editorial staff))
Published online: ((will be filled in by the editorial staff))

References

[1] B. Zhang, X. Zheng, O. Voznyy, R. Comin, M. Bajdich, M. García-Melchor, L. Han, J. Xu, M. Liu, L. Zheng, F. P. G. D. Arquer, C. T. Dinh, F. Fan, M. Yuan, E. Yassitepe, N. Chen, T. Regier, P. Liu, Y. Li, P. D. Luna, A. Janmohamed, H. L. Xin, H. Yang, A. Vojvodic, E. H. Sargent, *Science* **2016**, *352*, 333.

[2] X. Li, H. Liu, Z. Chen, Q. Wu, Z. Yu, M. Yang, X. Wang, Z. Cheng, Z. Fu, Y. Lu, *Nat. Commun.* **2019**, *10*, 1409.

[3] J. K. Hurst, *Science* **2010**, *328*, 315.

[4] R. D. L. Smith, M. S. Prévot, R. D. Fagan, Z. Zhang, P. A. Sedach, M. K. J. Siu, S. Trudel, C. P. Berlinguette, *Science* **2013**, *340*, 60.

[5] W. T. Hong, M. Risch, K. A. Stoerzinger, A. Grimaud, J. Suntivich, Y. Shao-Horn, *Energy Environ. Sci.* **2015**, *8*, 1404.

[6] M. S. Burke, L. J. Enman, A. S. Batchellor, S. Zou, S. W. Boettcher, *Chem. Mater.* **2015**, *27*, 7549.

[7] N. T. Suen, S. F. Hung, Q. Quan, N. Zhang, Y. J. Xu, H. M. Chen, *Chem. Soc. Rev.* **2017**, *46*, 337.

[8] B. Wurster, D. Grumelli, D. Hotger, R. Gutzler, K. Kern, *J. Am. Chem. Soc.* **2016**, *138*, 3623.

[9] L. Zhang, J. Xiao, H. Wang, M. Shao, *ACS Catal.* **2017**, *7*, 7855.

[10] H. Jiang, J. Gu, X. Zheng, M. Liu, X. Qiu, L. Wang, W. Li, Z. Chen, X. Ji, J. Li, *Energy Environ. Sci.* **2019**, *12*, 322.

[11] J. Hwang, R. R. Rao, L. Giordano, Y. Katayama, Y. Yu, Y. Shao-Horn, *Science* **2017**, *358*, 751.

[12] J. Yu, R. Ran, Y. Zhong, W. Zhou, M. Ni, Z. Shao, *Energy Environ. Mater.* **2020**, *3*, 121.

[13] J. Suntivich, K. J. May, H. A. Gasteiger, J. B. Goodenough, Y. Shao-Horn, *Science* **2011**, *334*, 1383.

[14] M. Risch, K. A. Stoerzinger, S. Maruyama, W. T. Hong, I. Takeuchi, Y. Shao-Horn, *J. Am. Chem. Soc.* **2014**, *136*, 5229.

[15] G. Li, S. Hou, L. Gui, F. Feng, D. Zhang, B. He, L. Zhao, *Appl. Catal. B Environ.* **2019**, *257*, 117919.

[16] E. Fabbri, M. Nachtegaal, T. Binninger, X. Cheng, B. J. Kim, J. Durst, F. Bozza, T. Graule, R. Schaublin, L. Wiles, M. Pertoso, N. Danilovic, K. E. Ayers, T. J. Schmidt, *Nat. Mater.* **2017**, *16*, 925.

[17] Y.-Q. Lyu, J. Yu, Z. Lu, F. Ciucci, *J. Power Sources* **2019**, *415*, 91.

[18] G. Chen, W. Zhou, D. Guan, J. Sunarso, Y. Zhu, X. Hu, W. Zhang, Z. Shao, *Sci. Adv.* **2017**, *3*, e1603206.

[19] F. Liang, Z. Yang, H. Deng, J. Sunarso, L. Yang, J. Mao, *J. Mater. Sci. Technol.* **2019**, *35*, 1184.

[20] D. Chen, C. Chen, Z. M. Baiyee, Z. Shao, F. Ciucci, *Chem. Rev.* **2015**, *115*, 9869.

[21] K. Zhu, F. Shi, X. Zhu, W. Yang, *Nano Energy* **2020**, *73*, 104761.

[22] Y. Zhu, L. Zhang, B. Zhao, H. Chen, X. Liu, R. Zhao, X. Wang, J. Liu, Y. Chen, M. Liu, *Adv. Funct. Mater.* **2019**, *29*, 1901783.

[23] D. Ji, L. Fan, L. Tao, Y. Sun, M. Li, G. Yang, T. Q. Tran, S. Ramakrishna, S. Guo, *Angew. Chem. Int. Ed.* **2019**, *58*, 13840.

[24] J. Xiong, H. Zhong, J. Li, X. Zhang, J. Shi, W. Cai, K. Qu, C. Zhu, Z. Yang, S. P. Beckman, H. Cheng, *Appl. Catal. B Environ.* **2019**, *256*, 117817.

[25] J.-I. Jung, M. Risch, S. Park, M. G. Kim, G. Nam, H.-Y. Jeong, Y. Shao-Horn, J. Cho, *Energy Environ. Sci.* **2016**, *9*, 176.

[26] J. Sun, Z. Zhang, Y. Gong, H. Wang, R. Wang, L. Zhao, B. He, *Sci. Rep.* **2019**, *9*, 4210.

[27] H. Wang, W. Xu, S. Richins, K. Liaw, L. Yan, M. Zhou, H. Luo, *Electrochim. Acta* **2019**, *296*, 945.

[28] L. Li, H. Yang, Z. Gao, Y. Zhang, F. Dong, G. Yang, M. Ni, Z. Lin, *J. Mater. Chem. A* **2019**, *7*, 12343.

[29] Q. A. Islam, R. Majee, S. Bhattacharyya, *J. Mater. Chem. A* **2019**, *7*, 19453.

[30] J.-I Jung, D. D. Edwards, *J. Solid State Chem.* **2011**, *184*, 2238.

[31] B. Hua, M. Li, Y.-Q. Zhang, Y.-F. Sun, J.-L. Luo, *Adv. Energy Mater.* **2017**, *7*, 1700666.

[32] Y. Wen, C. Zhang, H. He, Y. Yu, Y. Teraoka, *Catal. Today* **2007**, *126*, 400.

[33] H.-Y. Wang, Y.-Y. Hsu, R. Chen, T.-S. Chan, H. M. Chen, B. Liu, *Adv. Energy Mater.* **2015**, *5*, 1500091.

[34] D. K. Bediako, B. Lassalle-Kaiser, Y. Surendranath, J. Yano, V. K. Yachandra, D. G. Nocera, *J. Am. Chem. Soc.* **2012**, *134*, 6801.

[35] C. Hu, X. Wang, T. Yao, T. Gao, J. Han, X. Zhang, Y. Zhang, P. Xu, B. Song, *Adv. Funct. Mater.* **2019**, *29*, 1902449.

[36] P. Zeng, Z. Chen, W. Zhou, H. Gu, Z. Shao, S. Liu, *J. Membr. Sci.* **2007**, *291*, 148.

[37] X. Ding, Z. Gao, D. Ding, X. Zhao, H. Hou, S. Zhang, G. Yuan, *Appl. Catal. B Environ.* **2019**, *243*, 546.

[38] H. Lee, O. Gwon, K. Choi, L. Zhang, J. Zhou, J. Park, J.-W. Yoo, J.-Q. Wang, J. H. Lee, G. Kim, *ACS Catal.* **2020**, *10*, 4664.

[39] Y. Pan, X. Xu, Y. Zhong, L. Ge, Y. Chen, J. M. Veder, D. Guan, R. O'Hayre, M. Li, G. Wang, H. Wang, W. Zhou, Z. Shao, *Nat. Commun.* **2020**, *11*, 2002.

[40] S. She, J. Yu, W. Tang, Y. Zhu, Y. Chen, J. Sunarso, W. Zhou, Z. Shao, *ACS Appl. Mater. Interfaces* **2018**, *10*, 11715.

[41] S. She, Y. Zhu, Y. Chen, Q. Lu, W. Zhou, Z. Shao, *Adv. Energy Mater.* **2019**, *9*, 1900429.

[42] N.-I. Kim, Y. J. Sa, T. S. Yoo, S. R. Choi, R. A. Afzal, T. Choi, Y.-S. Seo, K.-S. Lee, J. Y. Hwang, W. S. Choi, S. H. Joo, J.-Y. Park, *Sci. Adv.* **2018**, *4*, eaap9360.

[43] H. Wang, J. Wang, Y. Pi, Q. Shao, Y. Tan, X. Huang, *Angew. Chem. Int. Ed.* **2019**, *58*, 2316.

[44] R. Zhang, N. Dubouis, M. B. Osman, W. Yin, M. T. Sougrati, D. A. D. Corte, D. Giaume, A. Grimaud, *Angew. Chem. Int. Ed.* **2019**, *58*, 4571.

[45] W. Wang, Y. Yang, D. Huan, L. Wang, N. Shi, Y. Xie, C. Xia, R. Peng, Y. Lu, *J. Mater. Chem. A* **2019**, *7*, 12538.

[46] B. Hua, M. Li, J.-L. Luo, *Nano Energy* **2018**, *49*, 117.

[47] Q. Luo, D. Lin, W. Zhan, W. Zhang, L. Tang, J. Luo, Z. Gao, P. Jiang, M. Wang, L. Hao, K. Tang, *ACS Appl. Energy Mater.* **2020**, *3*, 7149.

[48] J. Dai, Y. Zhu, Y. Yin, H. A. Tahini, D. Guan, F. Dong, Q. Lu, S. C. Smith, X. Zhang, H. Wang, W. Zhou, Z. Shao, *Small* **2019**, *15*, 1903120.

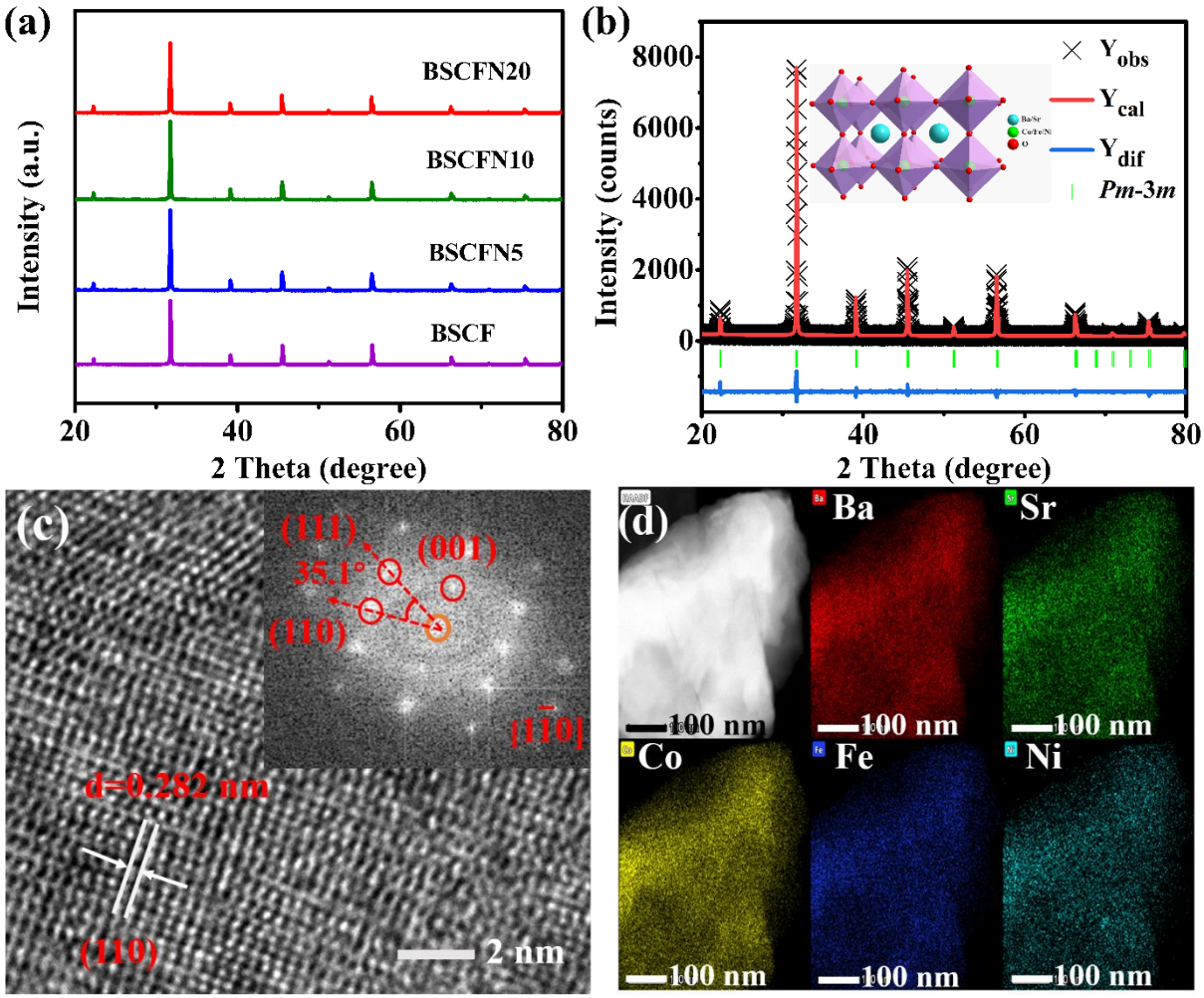

Figure 1. Crystalline structure of the electrocatalysts. a) XRD patterns of BSCFN*x* (*x* = 0~0.2), b) Rietveld-refined XRD profile of BSCFN20, c) HR-TEM image and corresponding FFT pattern (inset) of BSCFN20, d) EDX mappings of BSCFN20 sample.

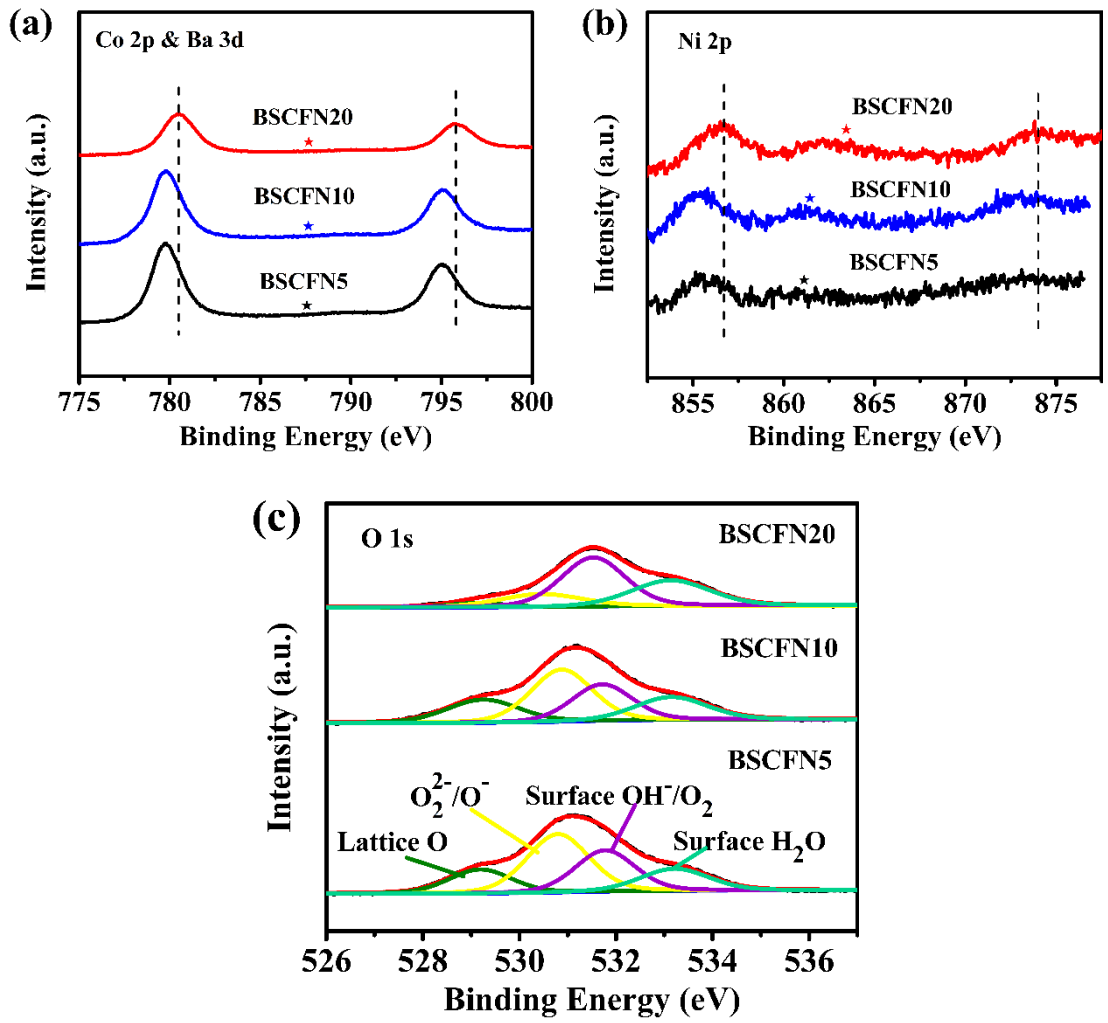

Figure 2. a) Co 2p and Ba 3d, b) Ni 2p, c) O 1s core-level XPS spectra of BSCFN*x*. Asterisks (★) indicate satellite peaks.

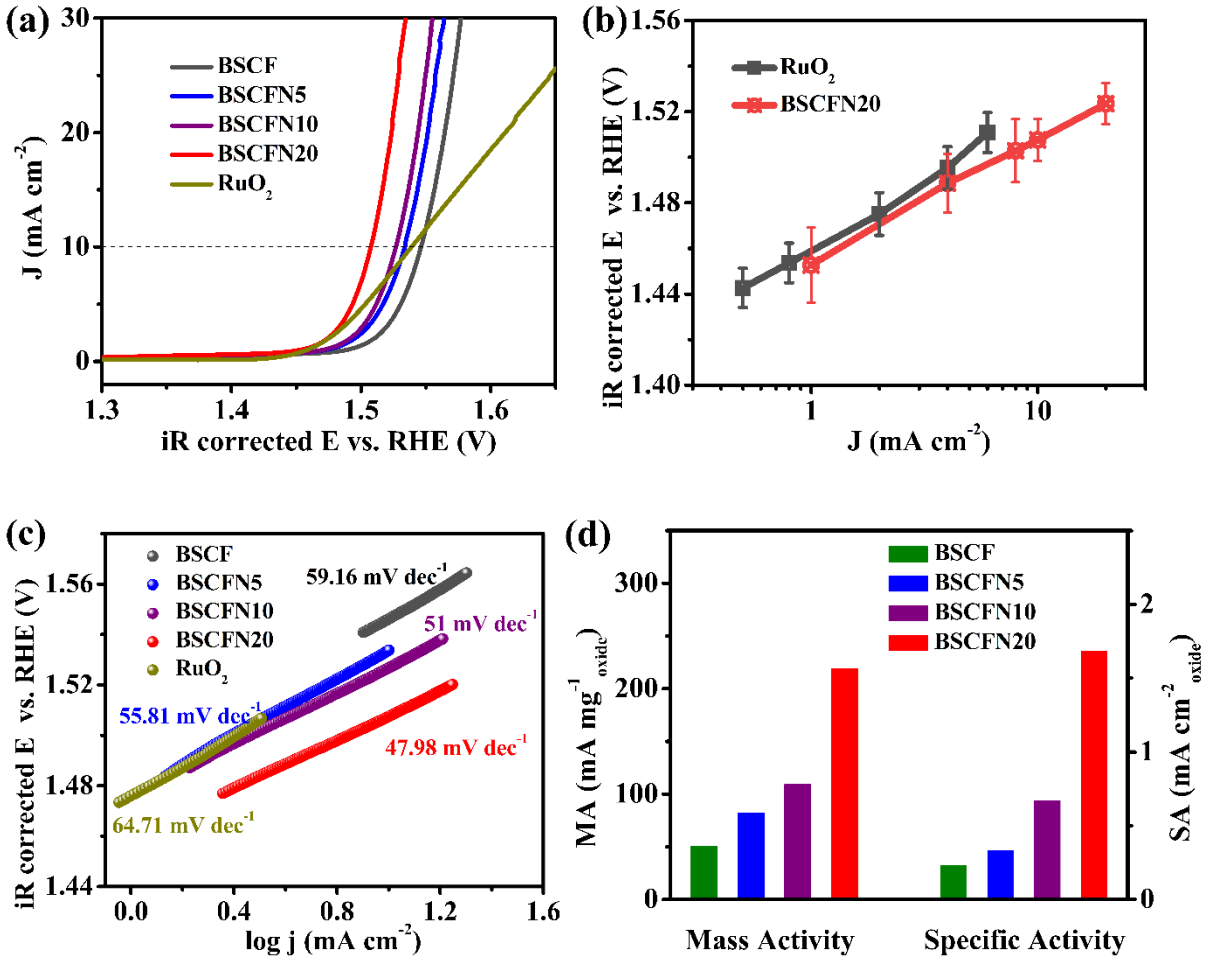

Figure 3. a) IR-corrected LSV curves of BSCFN*x* (*x* = 0~0.2) and commercial RuO_2, b) comparison of the intrinsic activity (current density) of BSCFN20 and RuO_2 on a logarithmic scale against potential, error bars represent standard deviation of the mean for at least three independent tests, c) Tafel plots toward OER of different catalysts, d) mass and specific activity of BSCFN*x* (*x* = 0~0.2) catalysts at an overpotential of 0.32 V.

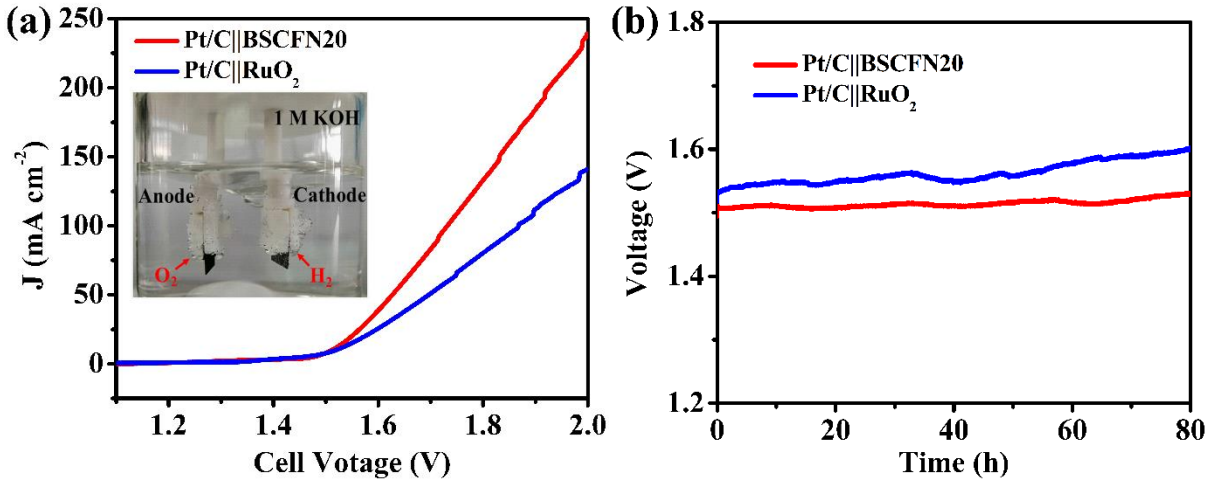

Figure 4. a) Polarization curves and b) chronopotentiometric curves of a two-electrode electrolyzer with Pt/C as a HER catalyst and BSCFN20 or RuO_2 as an OER catalyst for overall water splitting in 1 M KOH without iR compensation.

Table 1. Overpotential comparison of various perovskite electrocatalysts for OER at a current density of 10 mA cm^{-2}.

Catalyst	Electrolyte	RE [a)]	CE [b)]	Overpotential /mV	Ref.
$Bi_5CoTi_3O_{15}/BiCoO_3$	---	Ag/AgCl	Pt	387	2
$PrBa_{0.5}Sr_{0.5}Co_{1.5}Fe_{0.5}O_{5+\delta}$	1 M KOH	Ag/AgCl	Pt	~390	22
$Bi_{0.1}(Ba_{0.5}Sr_{0.5})_{0.9}Co_{0.8}Fe_{0.2}O_{3-\delta}$	0.1 M KOH	Hg/Hg_2Cl_2	Pt	370	26
$SrCo_{1-y}Si_yO_{3-\delta}$	0.1 M KOH	Ag/AgCl	Pt	417	39
$La_{0.2}Sr_{0.8}FeO_{3-\delta}$	0.1 M KOH	Ag/AgCl	Pt	370	40
$Sr(Co_{0.8}Fe_{0.2})_{0.7}B_{0.3}O_{3-\delta}$	0.1 M KOH	Ag/AgCl	Pt	340	41
$Nd_{1.5}Ba_{1.5}CoFeMnO_{9-\delta}$/N-rGO	1 M KOH	Hg/HgO	graphite	357	42
$LaFe_{0.2}Ni_{0.8}O_3$	1 M KOH	SCE	Pt	302	43
$Sr_2CoIr^{(V)}O_6$	0.1 M $HClO_4$	Ag/AgCl	Pt	330	44
$SrCoO_{2.85-\delta}F_{0.15}$	0.1 M KOH	Ag/AgCl	Pt	380	45
$La_{0.45}Sr_{0.45}Mn_{0.9}Fe_{0.1}O_{3-\delta}/Fe_3C/C$	0.1M KOH	Ag/AgCl	Pt	340	46
$Ba_{0.9}Sr_{0.1}Co_{0.8}Fe_{0.1}Ir_{0.1}O_{3-\delta}$	1.0 M KOH	Ag/AgCl	Pt	300	47
BSCFN20	**0.1 M KOH**	**Ag/AgCl**	**Pt**	**278**	**This work**

[a)] RE: reference electrode; [b)] CE: counter electrode.

Nickel-substituted perovskites $Ba_{0.5}Sr_{0.5}Co_{0.8-x}Fe_{0.2}Ni_xO_{3-\delta}$ (BSCFN*x*) are designed and developed as highly active and durable electrocatalysts for boosting oxygen evolution reaction (OER). With the Ni doping ratio increasing up to 20%, BSCFN20 exhibits the optimum OER activity, and alkaline electrolytic cell with BSCFN20 as an anode achieves remarkable activity and durability for water oxidation. The gradually increased oxygen vacancies resulting from the Ni substitution enables promising OER electroactivity, contributing to the advancement of water splitting.

Feifei Dong, Lu Li, Ziqi Kong, Xiaomin Xu, Yaping Zhang, Zhenghui Gao, Yangbiaokui Dong, Meng Ni, Quanbing Liu*, and Zhan Lin*

Materials Engineering in Perovskite for Optimized Oxygen Evolution Electrocatalysis in Alkaline Condition

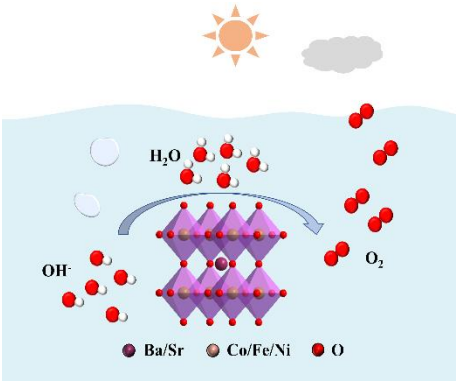

Supporting Information

Materials Engineering in Perovskite for Optimized Oxygen Evolution Electrocatalysis in Alkaline Condition

Feifei Dong, Lu Li, Ziqi Kong, Xiaomin Xu, Yaping Zhang, Zhenghui Gao, Yangbiaokui Dong, Meng Ni, Quanbing Liu, and Zhan Lin**

I. Experimental Section

Catalysts preparation: The perovskite catalysts including BSCF and BSCFN*x* were synthesized using a combined EDTA-citrate complexing sol-gel method as described previously.[1] After subjected to various high temperatures to form the desired phases, the resulting catalysts were ball-milled (Fritsch, Pulverisette 6) with ethanol as a solvent medium at 450 rpm for 10 h, followed by drying and grinding processes. The benchmark precious metal catalyst RuO_2 was purchased from Premetek company.

Catalysts characterization: Room-temperature X-ray diffraction pattern (XRD) of the synthesized perovskite powders were carried out on an X-ray diffractometer (Rigaku MiniFlex600, Cu Kα radiation, λ = 1.54059 Å) to determine the phase structure and purity. Detailed structural information, based on profile fitting of the XRD patterns, was obtained by GSAS-EXPGUI package.[2] High-resolution transmission electron microscopy (HR-TEM) images were conducted by Talos F200S. To evaluate the specific surface areas of the ball-milled catalysts, a Brunauer-Emmett-Teller (BET) analysis system (BELSORP-mini Ⅱ) with a N_2 adsorptive medium was performed. The surface valence of elements was acquired from X-ray photoelectron spectra (XPS, Thermo Fisher Escalab 250Xi). Binding energy of C 1s, located at 284.8 eV, was taken as the reference standard. The XPSPEAK41 software was employed for the peak fitting procedure. Iodometric titration method was applied to determine the oxygen non-stoichiometry (δ) of perovskite oxides at room temperature. The detailed experimental process can be available in our previous work.[3]

Electrochemical characterization: The electrochemical performance was measured by the combination of a CHI 760 electrochemical workstation and an RDE system (Pine Research Instruments). The working electrode, i.e. glassy carbon (GC) electrode, was pre-polished and rinsed before each test. A Pt wire and Ag/AgCl (saturated KCl) electrode acted as the counter and reference electrode, respectively. The saturated Ag/AgCl electrode was calibrated by the

reversible hydrogen electrode (RHE), resulting in the conversion equation: $E_{RHE} = E_{Ag/AgCl} + 0.993$ V. For preparation of catalyst-modified electrodes, 10 mg of perovskite oxides, 10 mg of carbon black (Super P Li), 100 μL of 5 wt. % Nafion solution, and 1 mL of ethanol were mixed and ultrasonically dispersed to generate a homogeneous suspension. Next, 5 μL of the resulting ink was drop-casted onto the surface of polished GC electrode (5 mm in diameter) followed by a natural drying process, yielding a catalyst mass loading of ~0.232 mg_{cat} cm^{-2}. The precious metal oxides RuO_2 catalyst was adopted as the reference with loading amount of ~0.116 mg_{cat} cm^{-2}. The 0.1 M KOH electrolyte was prepared by dissolving KOH pellets (99.99% weight, Aladdin) into a certain amount of ultrapure water (18 MΩ cm). The electrolyte was saturated by O_2 for at least 30 min before measurement and maintained O_2 saturation throughout OER test. Linear sweep voltammograms (LSVs) were detected on RDE under a rotating speed of 1600 rpm at a scan rate of 5 mV s^{-1} from 0.2 to 1.0 V (versus Ag/AgCl). To eliminate the effect of the solution resistance, all potential values reported here are iR-corrected using the following equation: $E_{iR\text{-}corrected} = E - iR$, where i is the measured current, while R represents ohmic resistance of electrolyte. For the determination of R value, electrochemical impedance spectroscopy (EIS) was conducted at 0.67 V with frequencies ranging from 100 kHz to 0.1 Hz under an AC voltage amplitude of 5 mV. Overall water splitting was carried out in a two-electrode system using BSCFN20 as an anode and commercial Pt/C as a cathode in 1.0 M KOH electrolyte. For comparison, the electrochemical behavior of commercial Pt/C||RuO_2 two-electrode configuration was also measured. Chronopotentiometry test was performed at a constant current density of 10 mA cm^{-2} to measure the durability of overall water splitting.

II. Supplementary Results

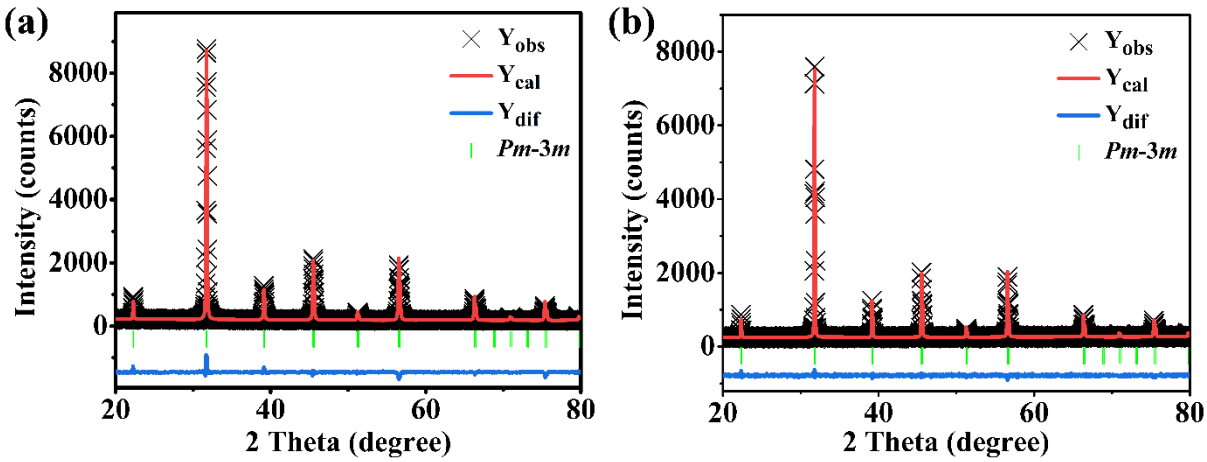

Figure S1. Rietveld-refined XRD profiles of a) BSCFN5 and b) BSCFN10.

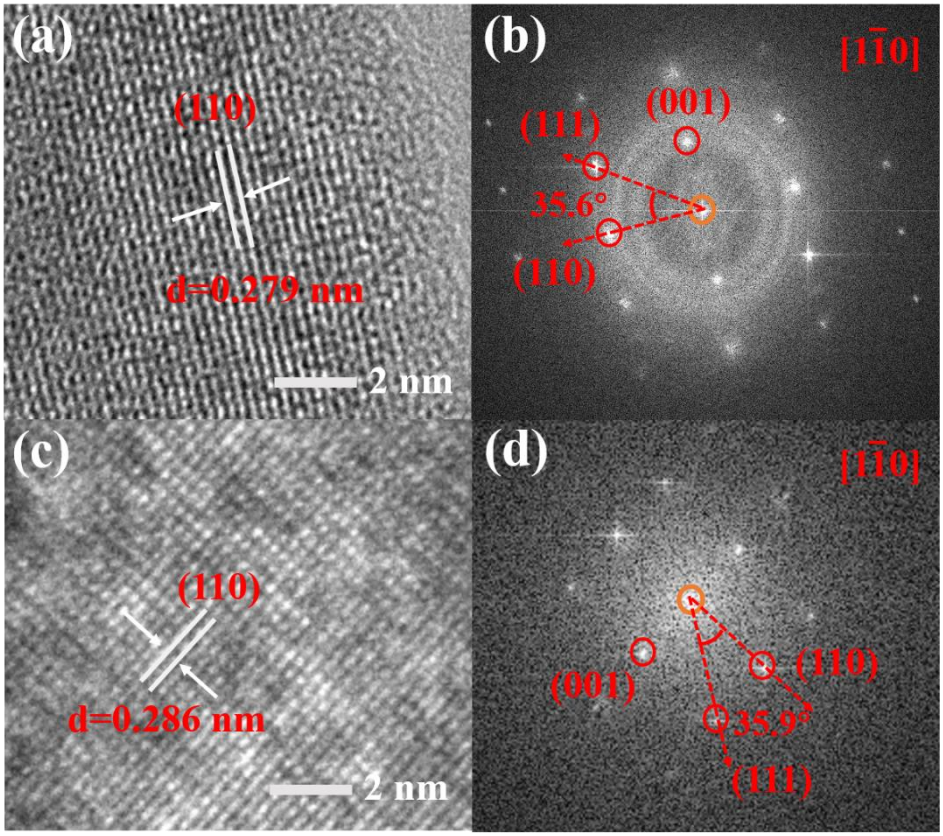

Figure S2. a) HR-TEM image and b) corresponding FFT pattern of BSCFN5, c) HR-TEM image and d) corresponding FFT pattern of BSCFN10.

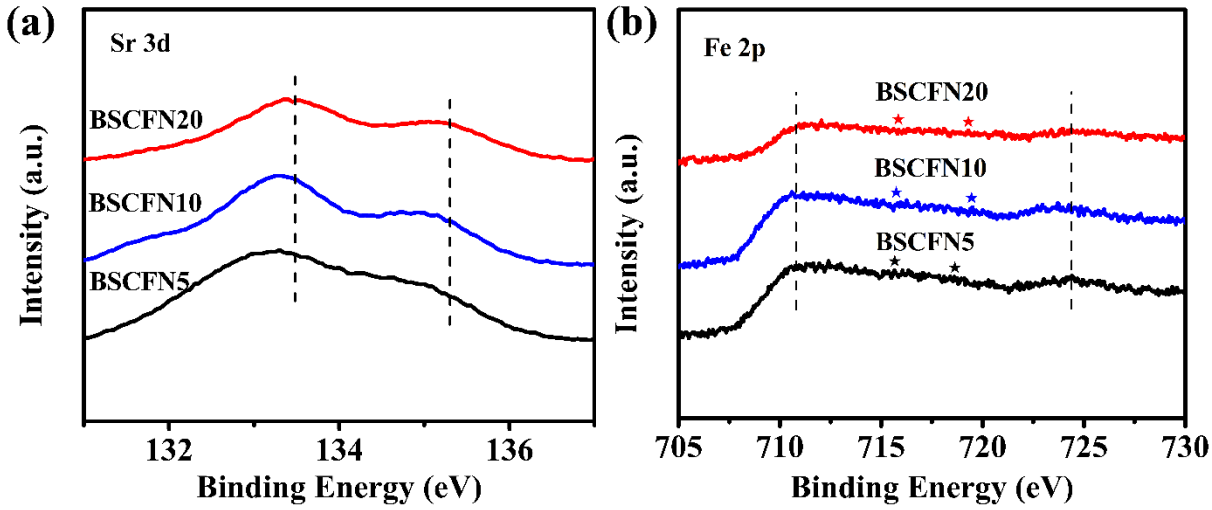

Figure S3. a) Sr 3d and b) Fe 2p core-level XPS spectra of BSCFN*x*. Asterisks (★) indicate satellite peaks.

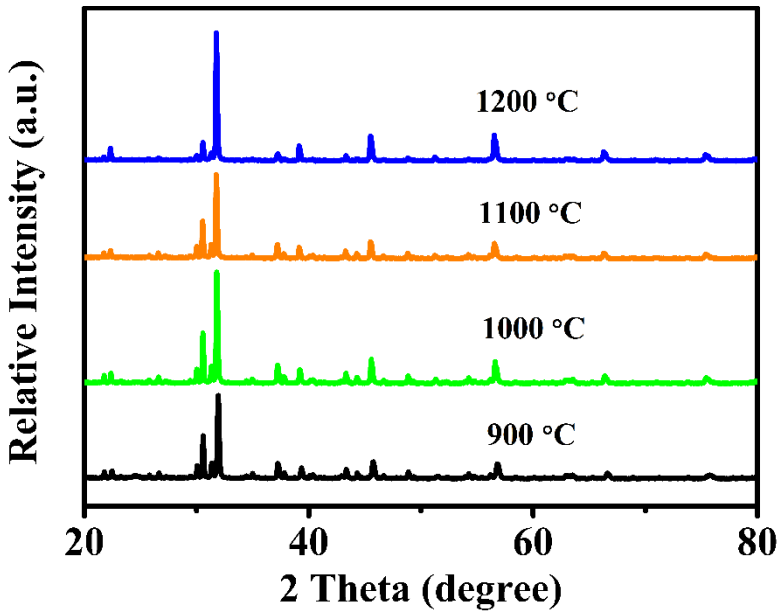

Figure S4. XRD patterns of BSCFN30 powder calcined at various temperatures.

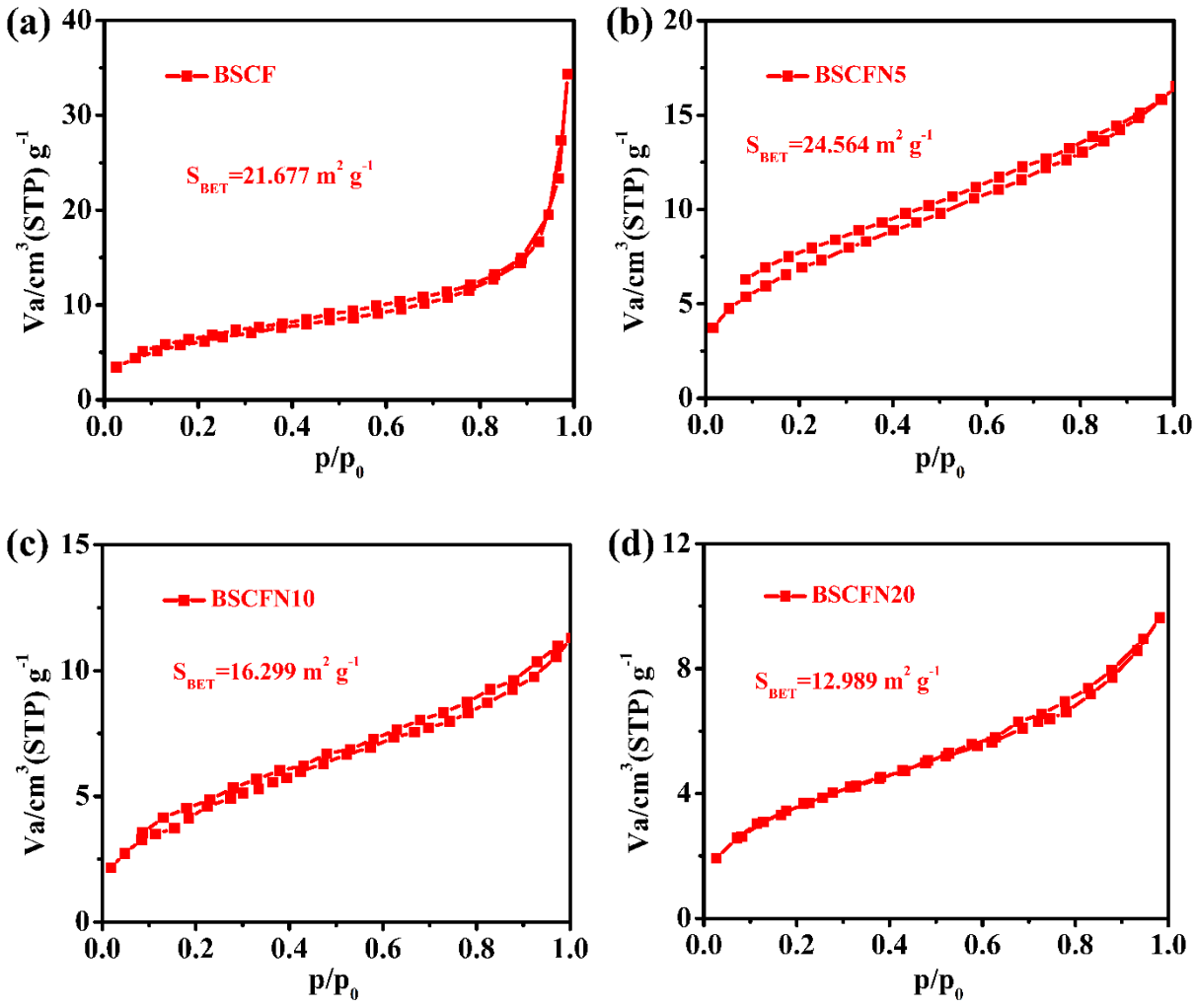

Figure S5. Nitrogen adsorption-desorption isotherm profiles of a) BSCF, b) BSCFN5, c) BSCFN10, and d) BSCFN20.

Table S1. Rietveld refinement results of XRD patterns of BSCFN*x* perovskites.

Perovskite	BSCFN5				BSCFN10				BSCFN20			
atom	*x*	*y*	*z*	occupancy	*x*	*y*	*z*	occupancy	*x*	*y*	*z*	occupancy
Ba	0.0	0.0	0.0	0.5083	0.0	0.0	0.0	0.5161	0.0	0.0	0.0	0.5074
Sr	0.0	0.0	0.0	0.4986	0.0	0.0	0.0	0.4992	0.0	0.0	0.0	0.5039
Co	0.5	0.5	0.5	0.7011	0.5	0.5	0.5	0.6932	0.5	0.5	0.5	0.6000
Fe	0.5	0.5	0.5	0.2000	0.5	0.5	0.5	0.1997	0.5	0.5	0.5	0.1997
Ni	0.5	0.5	0.5	0.099	0.5	0.5	0.5	0.1007	0.5	0.5	0.5	0.1990
O	0.5	0.5	0.0	0.8851	0.5	0.5	0.0	0.9517	0.5	0.5	0.0	0.8499
$Pm\bar{3}m$	a = 3.9833(7) Å				a = 3.9856(2) Å				a = 3.9832(5) Å			
R_{wp} (%)	6.55				6.15				6.59			
R_p (%)	5.00				4.82				4.99			
χ^2	1.064				1.101				0.905			

Supplementary References

[1] L. Li, H. Yang, Z. Gao, Y. Zhang, F. Dong, G. Yang, M. Ni, Z. Lin, *J. Mater. Chem. A* **2019**, *7*, 12343.

[2] B. H. Toby, *J. Appl. Crystallogr.* **2001**, *34*, 210.

[3] F. Dong, M. Ni, Y. Chen, D. Chen, M. O. Tadé, Z. Shao, *J. Mater. Chem. A* **2014**, *2*, 20520.